Carbon 181 (2021) 421–432

Contents lists available at ScienceDirect

Carbon

journal homepage: www.elsevier.com/locate/carbon

Research Article

Novel two-dimensional Group-IV carbides containing C_2 dimers: Sizable direct band gap, high carrier mobility, and anisotropic properties for nanoelectronics

Mehmet Emin Kilic *, Kwang-Ryeol Lee **

Computational Science Research Center, Korea Institute of Science and Technology, Seoul, 02792, Republic of Korea

ARTICLE INFO

Article history:
Received 16 March 2021
Received in revised form
23 April 2021
Accepted 28 April 2021
Available online 10 May 2021

Keywords:
2D carbides
Group-IV carbides
Tetrahexagonal carbides
Two-dimensional materials
Direct band gap semiconductors
Band gap engineering

ABSTRACT

Exploring novel materials with superior properties is of a great significance for potential applications in future electronics and optoelectronics. Based on first-principles calculations, we predict new two-dimensional (2D) group-IV carbides containing isolated C_2 dimers rather than individual carbon atoms, offering novel properties for nanoelectronics. The 2D carbides, namely *th*-XC_2 (X = Si, Ge, Sn, and so on), are not only dynamically, mechanically, and thermally stable, but also exhibit exceptional properties such as anisotropic elasticity, ideal strength, and tunable phononic band gap. Moreover, they are all narrow direct band gap semiconductors with band gaps up to ~0.9 eV, which can be continuously tuned by strain and alloy engineering. They show excellent transport properties including strong anisotropic and small electron/hole effective mass and ultrahigh carrier mobilities (up to $\sim 10^5 cm^2 V^{-1} s^{-1}$). Excitingly, the anisotropy of the hole effective mass can be rotated by 90° simply via alloying X element in tetrahexagonal carbon (*th*-C). Thus, the intrinsic carrier mobility in *th*-C is significantly enhanced by not only strain but also alloy engineering. In short, the 2D carbides are unique as composed of C_2 dimers with novel properties making them promising for nanoelectronics.

1. Introduction

Since the discovery of single layer-graphene [1], two-dimensional (2D) materials have attracted tremendous research interest. They have many natural advantages as high specific surface area, confined thickness in atomic scale, and other benefits, offering a wide range of material choices from semi-metals (e.g. graphene) to semiconductors (e.g. transition metal dichalcogenides TMDs [2] and recently discovered borophene [3]) and insulators (e.g. hexagonal boron nitride *h*-BN [4]), paving the way for designing high-performance nanoelectronic devices. To facilitate the device applications, robust stability to environment, sizable direct band gap, and high carrier mobility are of great importance. Considering the gapless of graphene and silicene [5], low carrier mobility of TMDs, and environmental instability of phosphorene [6], recently a race for finding new 2D materials is underway to overcome such limitations.

2D group-IV carbides (SiC, GeC, and SnC) are attractive as alternative materials for nanoscale electronic devices [7–10]. Zhou et al. predicted 2D graphene-like silicon carbide, namely siligraphene (*sili*-SiC_2), which possesses a direct band gap of 1.09 eV and holds promising for optoelectronic applications [11]. Shi et al. reported a series of graphene-like silicon carbides with Si partially replacing C atoms in graphene, exhibiting a rich variety of properties that go beyond those of graphene and silicene [12]. Not only theoretical prediction but also experimental observation [13] of 2D silicon carbides have triggered enormous interest in exploring novel 2D Si–C based nanomaterials such as *penta*-SiC_2 [14], silagraphene (*sila*-SiC_2) [15], and *sili*-SiC_7 [16].

Unlike individual C atoms, the C_2 dimers are an important structural unit in the growth of many carbon structures (fullerenes [17], nanotubes [18], and diamond [19]) and in the building of diverse carbon-based materials (Ti_mC_n metcars [20,21] and metal carbides [22,23]). More specifically, the C_2 dimers play a special role for the growing process of transition metal carbides. For instance, Joswig et al. reported the role of the C_2 units on the stability of Ti_mC_n metcars where the clusters containing C_2 dimers are energetically more favorable than those containing individual carbon

* Corresponding author.
** Corresponding author.
E-mail addresses: mekilic@kist.re.kr (M.E. Kilic), krlee@kist.re.kr (K.-R. Lee).

https://doi.org/10.1016/j.carbon.2021.04.092
0008-6223/

atoms or trimers [24]. In addition, from 2D titanium carbide (MXene) containing individual carbons to TiC_2 sheet containing C_2 dimers, a variety of novel properties (such as improved chemical stability, low mass density, high heat capacity, and remarkable Li storage capacity [22,23]) emerge, rendering the 2D materials with the C_2 dimers attractive for many applications.

Recently, a great effort has been devoted to study tetrahexagonal carbon (*th*-C), having robust stability and superior properties such as high carrier mobility and sizable band gap [25–27]. Very recently, we have predicted a series of group-IV carbides containing individual carbon atoms, exhibiting robust stability and remarkable properties such as sing-tunable Poisson's ratio, ultrahigh ideal strength, desirable band gaps, high carrier mobility, and visible-light absorption [28]. Stimulated by the special role of the C_2 dimers in the carbon-based materials, herein, we have extended the 2D tetrahex carbides family and explored new *th*-XC_2 (X = Si, Ge, Sn, and so on) tetrahex carbides containing C_2 dimers instead of individual C atoms. To evaluate the possibility and existence of the 2D carbides, we have investigated their energetic, dynamical, thermal, and mechanical stabilities by evaluating the formation energy, phonon dispersion curves, *ab-initio* molecular dynamics (AIMD) simulations, and elastic constants, respectively. Following the investigation on the stability, we have examined their exceptional properties, including anisotropic mechanical response, ideal strength, tunable phononic band gap, sizable direct electronic band gap, high carrier mobility, and anisotropic transport properties. Therefore, by means of simulation results we have clearly showed that the 2D carbides are attractive nanomaterials with potential application in the fields of nanoelectronics.

2. Methods

First-principle calculations were performed using density functional theory (DFT) within the generalized gradient approximation (GGA) in the form of Perdew-Burke-Ernzerhof (PBE) [29] as implemented the Vienna Ab-initio Simulation Package (VASP) [30]. The projector augmented wave (PAW) pseudopotentials were used to describe the electron-ion interactions [31,32]. A plane-wave basis with a cutoff energy of 520 eV was employed. The Brillouin zone (BZ) was sampled with a $21 \times 21 \times 1$ Γ-centered Monkhorst-Pack (MP) special *k*-point grids [33]. Since VASP always employes three dimensional (3D) periodic boundary conditions, a vacuum region of about 20 Å was applied along the *z*-direction to exclude the inter-sheets interactions. All geometric structures were fully relaxed until energy and forces were converged to 1×10^{-5} eV and 0.001 eV/Å, respectively. For the electronic calculations, we applied the Heyd-Scuseria-Ernzerhof (HSE06) functional method [34,35], which is known to well reproduce the experimental band gap value. For the lattice dynamics phonon calculations of the 2D carbides, the second order harmonic inter-atomic force constants were calculated using the Phonopy package [36]. Using a supercell approach ($4 \times 4 \times 1$ supercell with $2 \times 2 \times 1$ *k*-mesh), the phonon dispersion curves and phonon density of states (PhDOS) were computed from the force constants. The AIMD calculations were adopted to study the thermal stability of the 2D carbides, and performed within the NVT canonical ensemble where the temperature was controlled by Nose-Hover thermostat [37–39]. The AIMD simulation time was set for 6 ps with a time step of 1 fs at different temperatures.

To examine the Stone-Wales (SW) transformation in *penta*-SiC_2, the climbing-image NEB method [40] was used to find minimum energy paths (MEP) and transition states (TS) between the given initial state (IS) and final state (FS). The IS and FS were taken the same cell shape and volume. An interpolated chain of configurations (images) between IS and FS positions were connected by springs and relaxed simultaneously. The nine linearly interpolated images between IS and FS for the SW transformation were taken. All the images were relaxed until the maximum force acting on atom was less than 0.01 eVÅ^{-1}. The highest-energy image on the MEP will climb to the transition state.

3. Results and discussion

3.1. Structure characterization

The proposed 2D tetrahex carbides are formed entirely of tetragonal (*t*) and hexagonal (*h*) rings with three atomic layers where the top and bottom layers are only decorated with C=C dimers while the middle layer is only composed of X (Si, Ge, Sn) atoms. The unit cell (depicted as a red rectangle in Fig. 1) contains 12 atoms (4 X and 4 C_2) where each X atom is 4-fold coordinated with C_2 dimers. *th*-XC_2 (X = Si, Ge, Sn) carbides belong to the symmetry of *Cmma* (space group no 67), which is the same as *th*-C but different from the previously studied *th*-XC carbides [28] containing only X–C bonds and having the symmetry of *Pccm* (space group no 49). The predicted *th*-XC_2 carbides containing the C_2 dimers rather than individual carbon atoms are unique with alloying of group-IV element(s). For alloys 2D carbides, so-called ternary alloys, we studied the alloying of group-IV elements X (Si, Ge, Sn) with C_2 dimers where the same X atoms are placed on the certain line between C_2 dimers. Two different models were considered for the ternary alloys as the same X atoms are positioned along the zigzag direction (referred to as *th*-XC_2-zz shown in Fig. 1 (b)) and armchair direction (referred to as *th*-XC_2-ac shown in Fig. 1 (c)). The buckling thickness (*h*) is defined as the vertical difference between C_2 dimers at the top and bottom layers. The bond length d_1 and d_2 are defined for C=C and X–C, respectively.

The calculated structural parameters of *th*-XC_2 carbides are summarized in Table 1. For *th*-SiC_2, the optimized lattice constants, labeled as *a* and *b*, are $a = 5.52$ Å and $b = 7.20$ Å, higher than those of *th*-C as the radius of Si atom is larger than that of C atom. Moreover, the corresponding lattice parameters are lower than those of *th*-SiC ($a = 5.53$ Å and $b = 7.63$ Å) [28] due to high Si concentration. The C=C bond length (d_1) in *th*-SiC_2 is found to be 1.35 Å, which is slightly larger than that in *th*-C ($d_1 = 1.34$ Å), indicating pronounced character of carbon double bonds C=C. Moreover, the calculated Si–C bond length (d_2) about 1.90 Å is in the range of the standard Si–C bond length as 1.87–1.92 Å in *t*-SiC [41], 1.91 Å in *penta*-SiC_2 [14], and 1.92 Å in *sila*-SiC_2 [15] and comparable that in *th*-SiC ($d_2 = 1.88$ Å) [28]. The buckling thickness *h* of 1.34 Å is higher than that of *th*-C (1.16 Å) due to the larger Si–C bond length, exhibiting elongation in not only the in-plane direction but also the out-of-plane direction. In addition, the *h* of *th*-SiC_2 is lower than that of *th*-SiC (1.60 Å) due to the larger bond length of Si–C in *th*-SiC. We should note that Zhang et al. first predicted 46-SiC_2 structure using a bonding-restricted structure search method [42].

Likewise, the larger Ge–C bond length ($d_2 = 2.01$ Å) in *th*-GeC_2 lattice causes the elongation of the lattice in both in-plane and out-of-plane directions ($a = 5.93$ Å, $b = 7.34$ Å, and $h = 1.42$ Å). The d_2 in *th*-GeC_2 is almost same that in *th*-GeC (1.98 Å), tetragonal germanium carbide (*t*-GeC) (2.06 Å) and cubic germanium carbide (*c*-GeC) (2.01 Å) [28]. For *th*-SnC_2, the optimized lattice constants are $a = 6.59$ Å and $b = 7.94$ Å, which are considerably higher than those of *th*-C. The calculated Sn–C bond length of *th*-SnC_2 is about 2.23 Å, respectively, which is in the range of the standard Sn–C bond length (2.14–2.18) Å [43]. In general, the lattice constants are elongated with increasing the atomic number of X (X = Si, Ge, Sn). The d_1 in *th*-XC_2 carbides is found to be almost same as that of *th*-C. This indicates that the presence of constituent element (X) does not

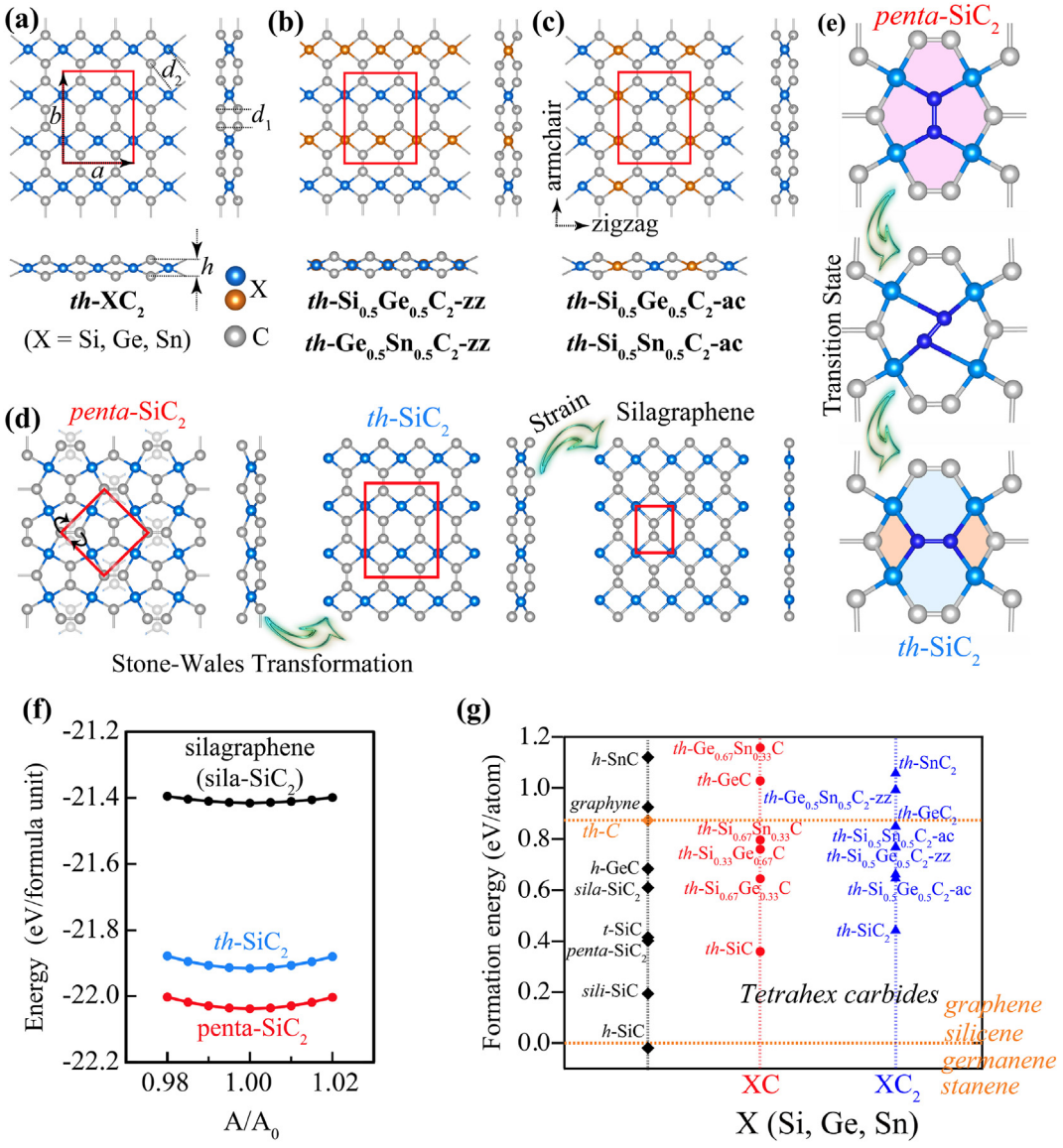

Fig. 1. Optimized atomic structures of *th*-XC_2 (X = Si, Ge, Sn) (a) and ternary alloys (b) and (c). Gray and sky blue/orange balls represent C and X atoms, respectively. Unit cells are framed by red line in the inset. (d) Structure formation mechanism from *penta*-SiC_2 to *th*-SiC_2 to *sila*-SiC_2. (e) TS between *penta*-SiC_2 and *th*-SiC_2 for the SW transformation. (f) Area dependence of the total energy for *th*-SiC_2, *sila*-SiC_2, and *penta*-SiC_2. (f) The relative formation energy of 2D carbides with respect to graphene, silicene, germanene, and stanene. (A colour version of this figure can be viewed online.)

Table 1
Optimized lattice constants (a and b), buckling thickness (h), bond lengths (d_1 for C=C and d_2 for X–C in Å), formation energies (E_f in eV), electronic band gaps (E_g^{PBE} and E_g^{HSE06} calculated from the PBE and HSE06 functional methods, respectively), and the band gap type.

	a (Å)	b (Å)	h (Å)	d_1 (Å)	d_2 (Å)	E_f (eV/atom)	E_g^{PBE} (eV)	E_g^{HSE06} (eV)	Type
th-C[a]	4.53	6.11	1.16	1.339	1.54	0.87	1.62	2.63	Direct
th-SiC_2	5.52	7.20	1.34	1.352	1.90	0.44	-	−0.01	Direct
th-GeC_2	5.93	7.34	1.42	1.339	2.01	0.85	0.17	0.87	Direct
th-SnC_2	6.59	7.94	1.42	1.331	2.23	1.06	-	0.15	Direct
th-$Si_{0.5}Ge_{0.5}C_2$-zz	5.74	7.25	$1.35^{h}{}_1$–$1.42^{h}{}_2$	1.35	$1.93^{b}{}_1$–$1.99^{b}{}_2$	0.66	-	0.53	Direct
th-$Ge_{0.5}Sn_{0.5}C_2$-zz	6.25	7.65	$1.36^{h}{}_1$–$1.51^{h}{}_2$	1.34	$2.07^{b}{}_2$–$2.18^{b}{}_3$	0.99	-	0.54	Direct
th-$Si_{0.5}Ge_{0.5}C_2$-ac	5.74	7.25	1.39	1.35	$1.90^{b}{}_1$–$2.02^{b}{}_2$	0.65	-	0.51	Direct
th-$Si_{0.5}Sn_{0.5}C_2$-ac	6.08	7.50	1.39	1.34	$1.91^{b}{}_1$–$2.22^{b}{}_3$	0.77	-	0.18	Direct

[a] Ref. 27. b_1, b_2, and b_3 superscripts indicate the d_2 bond length of Si–C, Ge–C, and Sn–C, respectively. h_1 and h_2 represent the minimum and maximum layer thickness, respectively.

affect the C=C bond length in *th*-XC_2. However, the d_2 bond length increases with increasing the atomic number of X. The change in the bond length of d_2 is attributed to the difference of atomic radius of C and X atoms, thereby the elongation of the lattice constants is mainly caused by the increase of the d_2. For the ternary alloying of *th*-$Si_{0.5}Ge_{0.5}C_2$-zz, the obtained corresponding structural

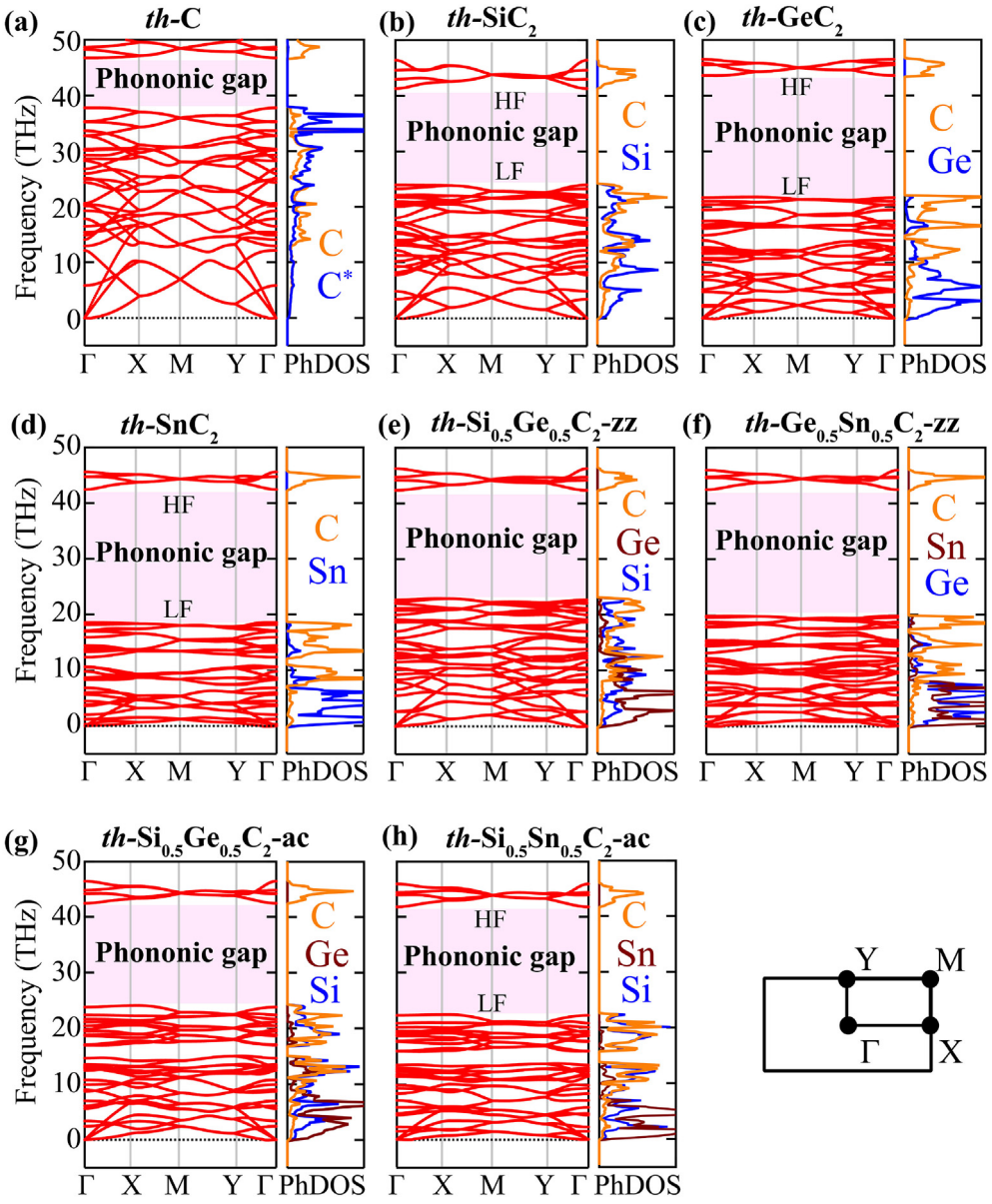

Fig. 2. Phonon dispersion curves along the direction of the Brillouin zone (BZ) (inset) and atom-projected density-of-states (PhDOS) of *th*-C (a), *th*-XC_2 (b)–(d), and ternary alloys (e)–(h). LF and HF refer to as the lower and higher frequency of the optical phononic gap (shaded by pink color), respectively. C and C* represent 3- and 4-fold coordinated carbon atoms, respectively. (A colour version of this figure can be viewed online.)

parameters are in between those of *th*-SiC_2 and *th*-GeC_2. Similar behavior is observed for all the proposed 2D ternary carbides. Thus, the alloying offers the ability to tailor the structural properties of *th*-XC_2 carbides.

3.2. Stability

3.2.1. Energetic stability

To describe the energetic stability of the 2D carbides, we performed the total-energy calculations. First, we compared the total energy of *th*-SiC_2 with other Si/C based materials having the same stoichiometry as SiC_2. According to our total-energy calculations, the predicted *th*-SiC_2 is found to be more stable than sila-graphene (*sila*-SiC_2) [15] and have slightly lower energetic state than *penta*-SiC_2 [14] as depicted in Fig. 1 (f). We noted that *th*-SiC_2 obviously is the buckled structure of silagraphene (Fig. 1 (d)). Indeed, it is known that 2D structures become energetically more favorable with increasing their buckling thickness, nearing close the bulk state. We further examined the possible structure formation mechanism of *th*-SiC_2 from the Cairo pentagonal silicon carbide (*penta*-SiC_2). We suggested that *th*-SiC_2 can be obtained by applying the SW transformation to *penta*-SiC_2. The SW transformation can be created by the 90° rotation of a C=C unit in *penta*-SiC_2 and consequently, transforming four pentagons into two tetragons and two hexagons (Fig. 1 (e)). The NEB results including the minimum-energy path (MEP) and the activation energy barrier for the SW transformation are presented in Fig. S1 of Supporting Information. The C=C bond length of 1.25 Å in TS is found to be lower than that in *penta*-SiC_2 (1.362 Å) and *th*-SiC_2 (1.35 Å). The shorter bond length of C_2 dimer in the TS indicates more double bond character, resulting in more strain and higher energy barrier. The calculated activation energy barrier of the SW transformation in *penta*-SiC_2 is found to be 2.98 eV. The formation of this transformation requires the re-formation and breaking of the bonds, resulting in high

energy barrier. Remarkably, however, the obtained energy barrier in *penta*-SiC_2 is much lower than the creation of the SW transformation in fullerene and graphene (about ~7–10 eV) [44,45]. Many efforts have been devoted to reduce the SW energy barrier by adding hydrogen [46], carbon [47], or metal atom [48]. We speculate that the SW transformation in metal-doped *penta*-SiC_2 would be more easily than that of the bare *penta*-SiC_2 owing to the electron donation and hybridization between the metal atom to *penta*-SiC_2. As for the formation of *sila*-SiC_2, we applied equi-biaxial tensile strain (~30%) to *th*-SiC_2 and observed it's purely planar structure formation, namely *sila*-SiC_2. As a benchmark, the optimized atomic structure of *penta*-SiC_2 and *sila*-SiC_2 is presented in Fig. S1 and Fig. S2 of Supporting Information, respectively.

Next, the energetic stability of the 2D carbides with respect to the experimentally realized group-IV monoelemental 2D materials including graphene, silicene, germanene, and stanene was determined by the formation energy difference $\Delta E_f = (E_{X_nC_m} - nE_X - mE_C)/(n + m)$, where $E_{X_nC_m}$ denotes the total energy of *th*-XC_2 carbides and E_X and E_C denote the sum energy of pure element of X = Si in silicene, X = Ge in germanene, X = Sn in stanene, and C in graphene, *n* and *m* refer to the total number of X and C atoms in the respective unit cell. The low ΔE_f value suggests the possibility of realizing the proposed 2D *th*-XC_2 carbides from the corresponding 2D materials. The calculated ΔE_f values, summarized in Table 1 and depicted in Fig. 1 (g), range from 0.44 eV/atom for *th*-SiC_2 to 1.06 eV/atom for *th*-SnC_2. These energies are comparable to that of *th*-XC carbides and some other 2D carbides. Considering the 2D graphdiyne having 0.85 eV formation energy, which has indeed been fabricated successfully, it might be feasible to realize the proposed 2D carbides on suitable substrates [49].

3.2.2. Dynamics stability and phononic band gap engineering

The dynamical stability of the 2D carbides was checked using the lattice dynamics calculations. Fig. 2 presents the calculated phonon band dispersion curves and atom-projected phonon density of states (PhDOS) of *th*-C, *th*-XC_2, and ternary alloys. According to the phonon dispersion curves, there is no imaginary phonon frequency in the whole BZ, which proves their dynamical stability.

The highest phonon frequency of *th*-C is found to be ~1700 cm^{-1}, which is higher than that of pentagraphene (~1600 cm^{-1}) [50] and *th*-BN (~1629 cm^{-1}) [51]. Likewise, the highest phonon frequency of *th*- (~1520 cm^{-1}) is higher than that of *penta*-SiC_2 (~1450 cm^{-1}) [14], *th*-SiC (~1100 cm^{-1}) [28], and *h*-SiC (~1000 cm^{-1}) [28]. The highest phonon frequency of *th*-GeC_2 (~1550 cm^{-1}) is higher than that of *th*-GeC (~930 cm^{-1}) [28], *t*-GeC (~750 cm^{-1}) [28], and *h*-GeC (~940 cm^{-1}) [28]. The highest frequency of *th*-SnC_2 (~1524 cm^{-1}) is found to be two times higher than that of *h*-SnC (780 cm^{-1}) [28]. Importantly, these obtained high frequency values confirm that the 2D carbides have very good kinetic stability and their bonds are rather robust.

Remarkably, the lattice dynamics calculations revealed that there exists a considerable phononic band gap in the phonon spectrum of *th*-C, *th*-XC_2, and ternary alloys, suggesting their potential application in phononic devices. The lower and higher frequency of the phononic band gap (depicted in Fig. 2) are referred to as LF and HF, respectively. For *th*-C, the phononic gap appears between LF (~1260 cm^{-1}) and HF (~1550 cm^{-1}). For *th*-SiC_2, the gap appears between ~810 cm^{-1} and ~1375 cm^{-1}. It is important to note that the LF is considerably shifted to lower frequency from *th*-C to *th*-SiC_2, while the HF is slightly shifted to lower frequency, resulting in a larger band gap. Likewise, the phonon gap for *th*-GeC_2 appears between ~725 cm^{-1} and ~1455 cm^{-1}. For *th*-SnC_2, the phonon gap appears between ~620 cm^{-1} and ~1408 cm^{-1}. In general, we observed that the position of LF is shifted to lower frequency from *th*-SiC_2 to *th*-SnC_2 whereas the HF is almost not changed. The PhDOS results clearly showed that the highest frequency modes are mainly characterized by the motion of carbon (C=C dimers) atoms while the lowest frequency modes are mainly contributed the vibration of X (Si, Ge, Sn) atoms. Hence, the LF and HF in *th*-XC_2 are mainly affected by the vibration of X and C atoms, respectively. It can be seen that the HF of *th*-XC_2 carbides and even ternary alloys is remained in the phonon spectrum. In our previous studies, we have found that the HF of *th*-C can be controlled by hydrogenations [27] or fluorinations [52]. Thus, the phononic gap (governed by LF and HF) in *th*-XC_2 can be effectively modulated by chemical functionalization/hybridization. On the other hand, from *th*-C to *th*-SnC_2, the decreasing of the LF can be explained in terms of two main factors: (i) the mass difference between C and X atoms and (ii) the chemical disorder. It is clear that replacing 4-fold coordinated carbon atoms (referred to as C^*) in *th*-C with other higher atomic mass atoms (Si, Ge, Sn) favors the creation of phononic gap. For instance, the large atomic mass difference between C and Si in *th*-SiC_2 leads to decrease the LS to lower frequency in the phonon spectrum and thereby create a very large phononic gap. We also noted that the increasing of atomic mass of X (X = Si, Ge, Sn) in *th*-XC_2 carbides causes much less dispersive phonon branches. Moreover, replacing 4-fold coordinated carbon atoms in *th*-C with Si atoms also introduces the chemical disorder since the Si–C (d_2 = 1.90 Å) is 19% longer than the $C^* - C$ bond d_2 = 1.54 Å. At this point, it is important to note that increasing the disorder further may results in the emergence of more phonon modes in the gap and thereby tend to disappear the phononic gap [28,53]. Based on the obtained results, it was concluded that the position and width of the phononic gap in the 2D carbides can effectively be tuned by hybridization and replacement of C^* with X atoms.

3.2.3. Thermal stability

Aiming to verify the thermal stability of the 2D carbides, the AIMD simulations were carried out using a larger 4 × 3 supercell (containing 144 atoms) at elevated temperatures. The potential energy of *th*-XC_2 and ternary alloys as a function of simulation time is shown in Fig. S3 of Supporting Information. It can be seen that there is only very small fluctuations of energy around the thermally equilibrium with time during the simulations. From the monitored

Table 2
Calculated elastic constants (C_{ij}) in N/m, Young's modulus (Y) in N/m and Poisson's ratio (ν) for in-plane deformations along the zigzag and armchair directions, and ultimate tensile strength (UTS) in % along the zigzag, armchair, and biaxial directions for *th*-C, *th*-XC_2, and ternary alloys.

	C_{11}	C_{22}	C_{12}	C_{66}	Y_{zigzag}	$Y_{armchair}$	ν_{xy}	ν_{yx}	UTS_{zigzag}	$UTS_{armchair}$	$UTS_{biaxial}$
th-C[a]	287.03	280.82	16.21	123.99	286.12	279.88	0.06	0.06	32	31	20
th-SiC_2	99.85	104.47	45.03	55.94	79.55	85.06	0.45	0.43	27	26	20
th-GeC_2	125.36	112.22	14.17	47.93	123.76	110.43	0.11	0.13	18	18	13
th-SnC_2	88.80	68.35	14.51	21.79	86.42	65.27	0.16	0.21	13	19	12
th-$Si_{0.5}Ge_{0.5}C_2$-zz	112.78	101.56	34.35	50.50	102.32	89.94	0.30	0.34	23	22	18
th-$Ge_{0.5}Sn_{0.5}C_2$-zz	95.68	80.60	18.49	30.41	92.10	76.36	0.19	0.23	15	21	13
th-$Si_{0.5}Ge_{0.5}C_2$-ac	110.87	100.62	34.27	51.02	100.28	88.95	0.31	0.34	16	26	23
th-$Si_{0.5}Sn_{0.5}C_2$-ac	100.00	84.14	28.44	31.06	91.92	74.52	0.28	0.34	21	26	20

[a] Ref. [27].

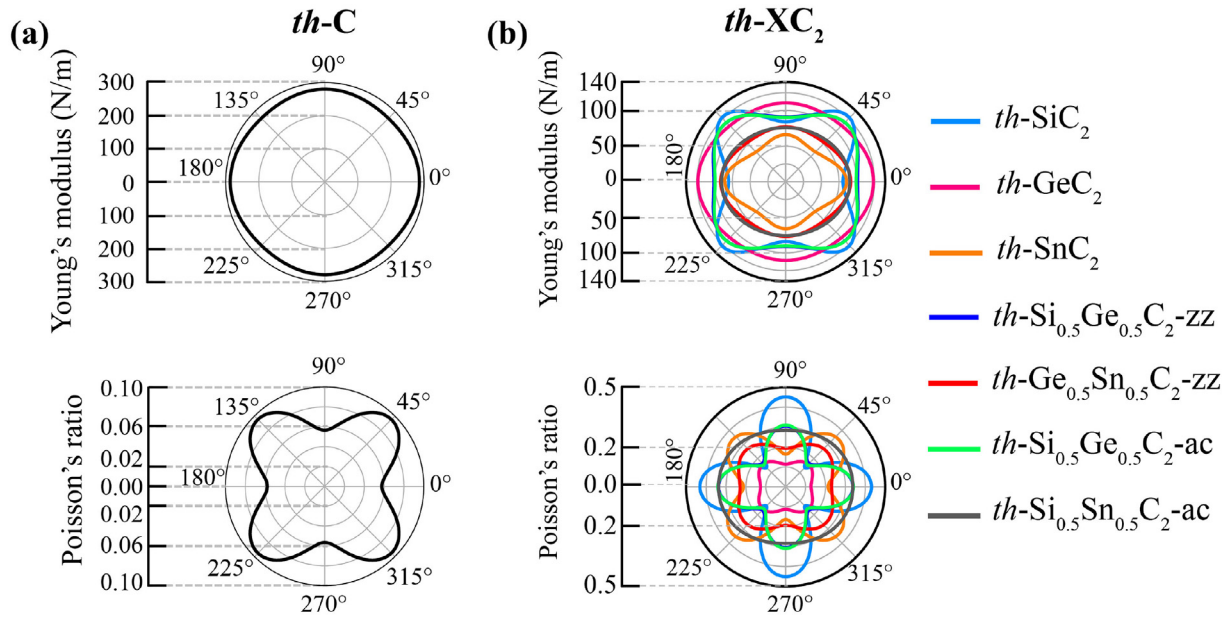

Fig. 3. (Upper panel) Angle dependent Young's modulus $Y(\theta)$ and Poisson's ratio $\nu(\theta)$ of (a) *th*-C and (b) *th*-XC_2 and ternary alloys. (A colour version of this figure can be viewed online.)

atomic configurations at the end of the simulation time, the integrity of the original configurations is maintained. Thus, the 2D carbides remain intact without any structural re-formation under the corresponding thermal shock, and thereby confirming their thermal stability.

3.2.4. Mechanical stability

We finally tested the mechanical stability of the 2D carbides in terms of the Born-Huang elastic stability criteria [54] as $C_{11}C_{22}-C_{12}^2>0$ and $C_{66}>0$ where C_{ij} is the in-plane elastic stiffness constants determined from strain energy (E_s) due to the existence of the axial strains. The strain energy per unit area in *th*-C, *th*-XC_2, and ternary alloys is calculated as:

$$E_s(\varepsilon)=\frac{1}{2}C_{11}\varepsilon_x^2+\frac{1}{2}C_{22}\varepsilon_y^2+C_{12}\varepsilon_x\varepsilon_y+2C_{66}\varepsilon_{xy}^2 \quad (1)$$

where ε_{ij} is the corresponding infinitesimal strain defined as $\varepsilon_i=(L_i'-L_i)/L_i$ $(i=x,y)$ where L_i' and L_i are the strained and unstrained lattice parameters (in Voigt notations as $1\equiv xx$; $2\equiv$ yy; $6\equiv$ xy). The first and second derivatives of the strain energy describe force and stiffness terms, respectively. Using the second derivatives of the strain energy with respect to the axial tensile and compressive strains (ε_i, i = 1, 2,), the corresponding elastic constants can be derived from Eq. (1) as

$$\text{for zigzag strain} \rightarrow (\varepsilon_y,\varepsilon_{xy}=0), E_s(\varepsilon)=\frac{1}{2}C_{11}\varepsilon_x^2 \quad (2)$$

$$\text{for armchair strain} \rightarrow (\varepsilon_x,\varepsilon_{xy}=0), E_s(\varepsilon)=\frac{1}{2}C_{22}\varepsilon_y^2 \quad (3)$$

$$\text{for biaxial} \rightarrow (\varepsilon_x=\varepsilon_y), (\varepsilon_{xy}=0), E_s(\varepsilon)=\left(\frac{1}{2}C_{11}+\frac{1}{2}C_{22}+C_{12}\right)\varepsilon_x^2 \quad (4)$$

$$\text{for shear strain} \rightarrow (\varepsilon_x,\varepsilon_y=0), E_s(\varepsilon)=2C_{66}\varepsilon_{xy}^2 \quad (5)$$

The strain energy curves of *th*-C, *th*-XC_2, and ternary alloys with respect to uniaxial (zigzag and armchair), biaxial, and shear strains are plotted in Fig. S4 of Supporting Information. The obtained elastic constants of the 2D carbides, summarized in Table 2, obey the mechanical stability criteria accordingly, confirming their mechanically stability.

3.3. Mechanical properties

Having confirming the great energetic, dynamical, thermal, and mechanical stability of the 2D carbides, we systematically studied their mechanical properties. The elastic constants play an important role for the determination of the elastic material properties such as Young's modulus and Poisson's ratio. First of all, we calculated the directional behavior of Young's modulus Y and Poisson's ratio ν for *th*-C, *th*-XC_2, and ternary alloys using the following expressions:

$$Y(\theta)=\frac{C_{11}C_{22}-C_{12}^2}{C_{11}s^4+C_{22}c^4+\left(\frac{(C_{11}C_{22}-C_{12}^2)}{C_{66}}-2C_{12}\right)s^2c^2} \quad (6)$$

$$\nu(\theta)=\frac{C_{12}(s^4+c^4)-\left(C_{11}+C_{22}-\frac{(C_{11}C_{22}-C_{12}^2)}{C_{66}}\right)s^2c^2}{C_{11}s^4+C_{22}c^4+\left(\frac{(C_{11}C_{22}-C_{12}^2)}{C_{66}}-2C_{12}\right)s^2c^2} \quad (7)$$

where $s=\sin(\theta)$ and $c=\cos(\theta)$. It is expected that the 2D carbides exhibit anisotropic mechanical responses due to their unique atomic structure. Fig. 3 shows the polar diagrams of Y and ν as a function of angle, confirming the strong anisotropic mechanical behavior in the 2D carbides. The calculated Y and ν of *th*-C, *th*-XC_2, and ternary alloys are summarized in Table 2. The Young's modulus of *th*-SiC_2 is found to be 79.55 N/m and 85.06 N/m along zigzag and armchair directions, respectively, which are lower than that of *th*-SiC (Y_{zigzag} = 143.53 N/m and $Y_{armchair}$ = 107.29 N/m [28]). The

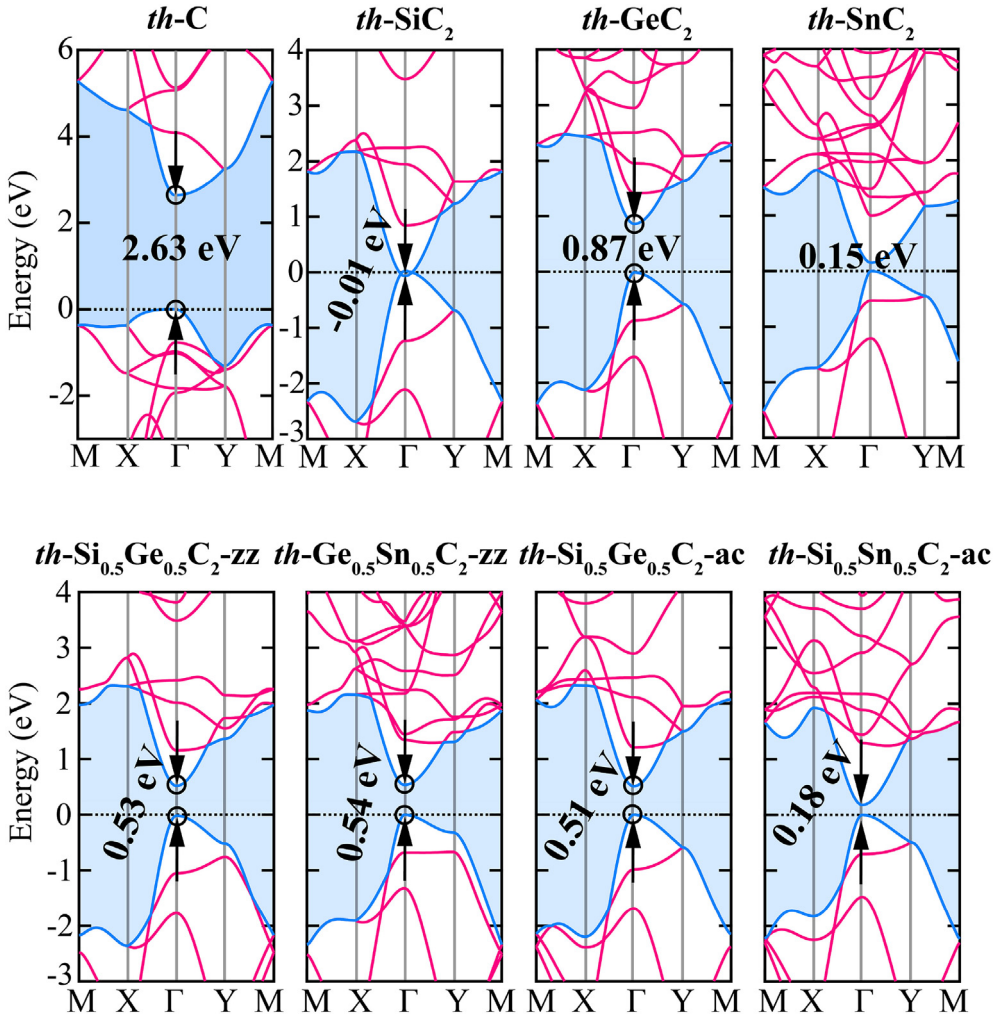

Fig. 4. Electronic band structures of *th*-C, *th*-XC_2, and ternary alloys (obtained from the HSE06 method). The Fermi level is set to zero and marked by black dashed lines. (A colour version of this figure can be viewed online.)

calculated Young's modulus of *th*-GeC_2 (Y_{zigzag} = 123.76 N/m and $Y_{armchair}$ = 110.43 N/m) is higher than that of *th*-GeC (Y_{zigzag} = 118.83 N/m and $Y_{armchair}$ = 83.72 N/m [28]). The predicted Young's modulus of *th*-SnC_2 are about Y_{zigzag} = 86.42 N/m and $Y_{armchair}$ = 65.27 N/m. For ternary alloys, the Young's modulus of *th*-$Si_{0.5}Ge_{0.5}C_2$-zz and *th*-$Si_{0.5}Ge_{0.5}C_2$-ac are almost same values, indicating that the distribution of X (Si and Ge) atoms is not significant on the Young's modulus of *th*-XC_2 carbides. Importantly, the Young modulus values of *th*-$Si_{0.5}Ge_{0.5}C_2$-zz and *th*-$Si_{0.5}Ge_{0.5}C_2$-ac are in between that of *th*-SiC_2 and *th*-GeC_2, indicating the ability to engineer the mechanical properties by alloying. We note that the low Young's modulus of the 2D carbides ensures their flexibility [55] and stretchability with respect to *th*-XC [28]. Furthermore, unlike the auxetic tetrahexagonal AlN [55], the Poisson's ratio (PR) of *th*-XC_2 and ternary alloys listed in Table 2 is a positive constant (non-auxetic) ranging from 0.11 to 0.45, which are higher than that of the *th*-C (0.06) [27], *th*-XC carbides (0.02–0.07) [28], and *th*-BN (0.02) [51].

We further examined their ability to withstand large tensile strains without failure, which is important for low dimensional nanomaterials [56,57]. The 2D carbides with 2 × 2 supercell were subjected to zigzag, armchair, and equi-biaxial in-plane strains up to ~25–30% in steps of 1%, and the corresponding stresses were calculated. We plotted the stress-strain relations for *th*-XC_2 and ternary alloys under zigzag, armchair, and biaxial tensions in Fig. S5 of Supporting Information. It can be readily seen that for small strain, the stress for the 2D carbides exhibits linear dependence on the applied strain for zigzag, armchair, and biaxial tensions. For further strains, the stress continues to increase to reaches the maximum stress, termed the ultimate tensile strength (UTS) and the corresponding strain is termed the ultimate strain. The obtained UTS values of *th*-XC_2 and ternary alloys given in Table 2 are found to be lower than those of *th*-C (32% zigzag, 31% armchair, and 20% biaxial), *th*-BN (32% zigzag, 36% armchair, and 27% biaxial) [51], and *th*-AlN (40% zigzag, 35% armchair, and 26% biaxial) [55].

3.4. Electronic properties

We further investigated the electronic properties of the 2D carbides. Fig. 4 presents the electronic band structures of *th*-C, *th*-XC_2, and ternary alloys at the HSE06 method. The calculated electronic band gap energies obtained from the PBE and HSE06 methods are listed in Table 1. According to the PBE scheme, the 2D carbides, except for *th*-C and *th*-GeC_2 having band gap energy of 1.62 eV and 0.17 eV, respectively, present metallic properties since there is no band gap. It is well-known that the PBE functional considerably underestimates the band gap of semiconductors. The actual value of the band gap is expected to be larger than the

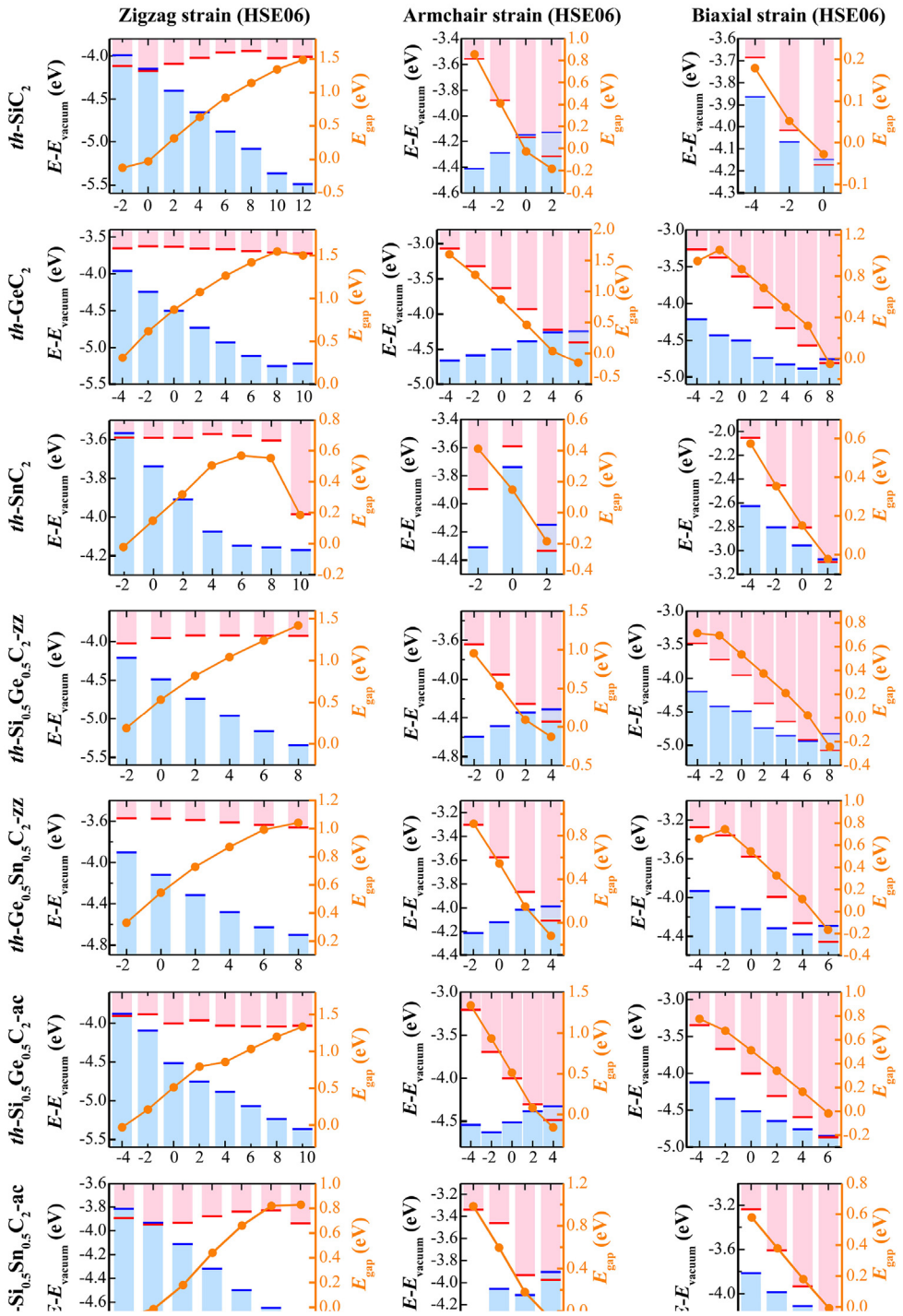

Fig. 5. Variation of absolute positions of band edges with respect to vacuum level and band gap energy as a function of zigzag (left panels), armchair (middle panels), and biaxial (right panels) strains. The energy level of vacuum is set to 0 eV. Blue and red lines represent the VBM and CBM energies, respectively; orange markers represent the band gap energy value. (A colour version of this figure can be viewed online.)

calculated band gap value at the PBE functional. According to the HSE06 scheme, all the 2D carbides, except for *th*-SiC_2 exhibiting a semimetal-like band structure with a near zero band gap (about −0.01 eV) and *th*-*C* having a relatively large band gap (about 2.63 eV), are semiconductors with narrow direct band gaps up to 0.87 eV as the VBM and CBM are located at the Γ point of the BZ. It is worthy of note that we are most likely not far off the real gap value with the results of the HSE06 method. The atom and orbital projected density of states (pDOS) is further calculated to get more insight into the electronic properties of the 2D carbides (Fig. S6 of Supporting Information). From the pDOS analysis, the states near the valence- and conduction-band edges have the *p* orbitals of C atoms. Such a conclusion can be drawn from the analysis of the partial charge density corresponding to band edges (Fig. S7 of Supporting Information). The charge densities of 2D carbides are of similar feature and localized at the sp^2-hybridized C═C bonds,

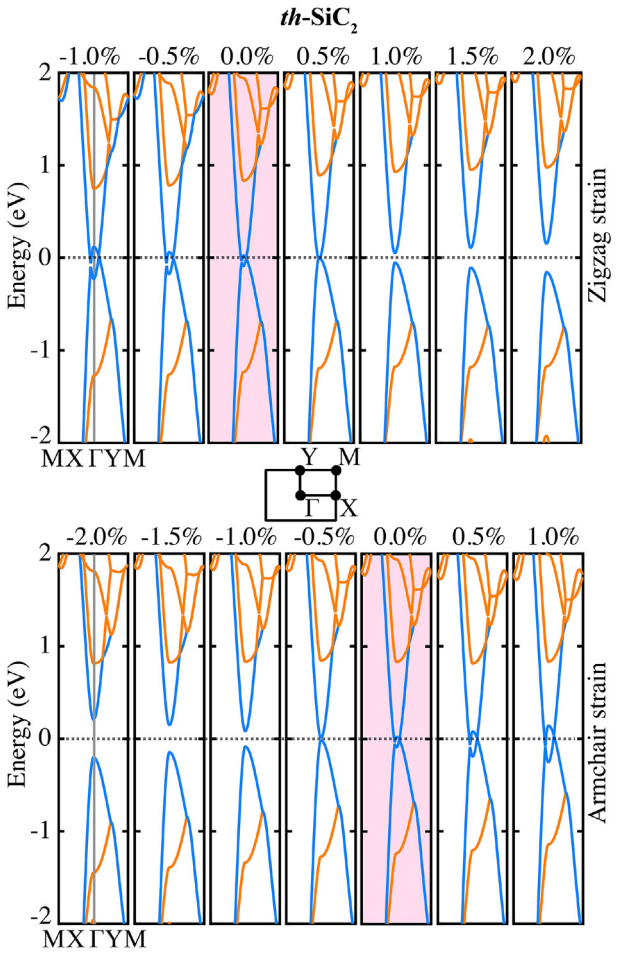

Fig. 6. Electronic band structure of *th*-SiC_2 as a function of zigzag and armchair strains (without SOC). The zero of energy is set to the Fermi level. Sky blue color lines represent the VBM and CBM. (A colour version of this figure can be viewed online.)

which results from the charge transfer from the X element to C atom arising from the strong 2*p* of C when the X–C bond is formed. To examine the bond feature, we plotted the electron localization function (ELF) in Fig. S8 of Supporting Information. An iso-surface of the ELF exhibits two domains: one is the bonding between adjacent C–C (σ and π bonds) and the other is the electron localization occurs around the center of X and C, suggesting mostly covalent character. The existence of sp^2-hybridized C=C bonds and the covalent X–C bonds play a crucial role in the stabilization of *th*-XC_2 structures.

3.4.1. Band gap engineering by alloying

Verifying great distinct stability and examining the effect of alloying on their structure and mechanical properties, we introduced the strategy to engineer the electronic direct band gaps of the 2D carbides by alloying. The *th*-SiC_2 exhibits a near zero direct band gap (-0.01 eV) and behaves like a conductor, may limit its applications. It is found that the band gap of the *th*-SiC_2 is enhanced by alloying other group-IV elements such as germanium or tin. Such that the band gap of *th*-$Si_{0.5}Ge_{0.5}C_2$-zz (0.53 eV), *th*-$Si_{0.5}Ge_{0.5}C_2$-ac (0.51 eV), and *th*-$Si_{0.5}Sn_{0.5}C_2$-ac (0.18 eV) indicated that germanium and tin within the *th*-SiC_2 is able to open the band gap. Likewise, the band gap of *th*-GeC_2 decreases by alloying silicon or tin and that of the *th*-SnC_2 increases by alloying silicon. Therefore, the electronic properties of *th*-XC_2 carbides can be tuned by alloy engineering. It is important to note that the alloying does not change the intrinsic and desirable direct band gap feature of *th*-XC_2 carbides.

3.4.2. Band gap engineering by strain

Another effective way to module the electronic properties of nanomaterials is strain engineering [55]. We systematically investigated the effect of strain on the electronic structures of the 2D carbides at the HSE06 method. Fig. 5 shows the variation of band gap and band edge positions of *th*-XC_2 and ternary alloys with respect to zigzag, armchair, and biaxial strains (tensile and compression). Obviously, we observed that the transitions, including from the metal to direct band gap semiconductor and the direct band gap semiconductor to metal, occur by strain engineering, depending on the direction and rate of strain. For instance, at very small strain (0.5% strain along the zigzag direction or ~-0.5% strain along the armchair direction), *th*-SiC_2 with band gap of 0.00 eV at the HSE06 method shows a semi-metallic characteristic. For further strains, the *th*-SiC_2 is found with an opened direct band gap of 0.10 eV at 1% zigzag strain, 0.17 eV at −1% armchair strain, and 0.05 eV at −2% biaxial strain. It is worth noting that when *th*-SiC_2 is subjected to compressive strain along the zigzag direction (or tensile strain along the armchair direction), the band inversion between VBM and CBM takes place in the vicinity of the Γ point as shown in Fig. 6, which is also confirmed by the charge distribution of VBM and CBM (Fig. S7 of Supporting Information). Here, we examined the strain-driven band inversion in the vicinity of the Fermi level rather than spin-orbit coupling (SOC) [58]. The band inversion may suggest that the *th*-SiC_2 has a topological order. In general, the electronic band gap of the 2D carbides increases with zigzag tensile strain where the sizable band gap change is mainly induced by the change of the VBM. For armchair and biaxial strains, we observed that the band gap energy decreases with increasing strain. These results revealed that the zigzag strain is efficient for the band gap opening whereas the armchair strain introduces the band gap closing behavior in the 2D carbides. It is worthy noting that, the nature of direct band gap of the 2D carbides still maintain under the corresponding strains. Remarkably, the sizable direct band gap feature makes the 2D carbides promising candidates for nano- and opto-electronics.

3.4.3. Small effective mass and high carrier mobility

We further examined the effective mass and carrier mobility of the 2D carbides, which are of great significance to the carrier transport properties of semiconductor nanomaterials [55]. The effective mass m^* of electron and hole is calculated in different directions by fitting the electronic band structures (obtained from the HSE06 method) according to the following equation: $m^* = \hbar^2(d^2E(k)/dk^2)^{-1}$ where $E(k)$ is the band-edge eigenvalue, k is the wave-vector, and $\hbar$ is the reduced Planck constant. The direction dependent effective mass of electron (m_e^*) and hole (m_h^*) for *th*-C, *th*-XC_2, and ternary alloys from Γ-X to Γ-A (where A is an arbitrary direction) is plotted in Fig. 7 and summarized in Table 3. We found that *th*-C and *th*-XC_2 carbides exhibit the same positions of the CBM and different position of the VBM. Considering the different shape of the hole effective mass between *th*-C and *th*-XC_2, the hole carrier transport direction in *th*-C can be rotated by 90° when substituting 4-fold carbon atoms with group-IV element(s) of Si, Ge, and Sn, which is desirable for nano-electronic device applications. That is, the anisotropy of the hole effective mass can be rotated by 90° simply by alloying X element in *th*-C. Thus, the intrinsic carrier mobility of the *th*-C is significantly enhanced by not only strain [59] but also alloy engineering. For *th*-XC_2 carbides, the hole effective mass along the Γ-X (ranging from 0.06 m_0 to 0.11 m_0, m_0 is the free-

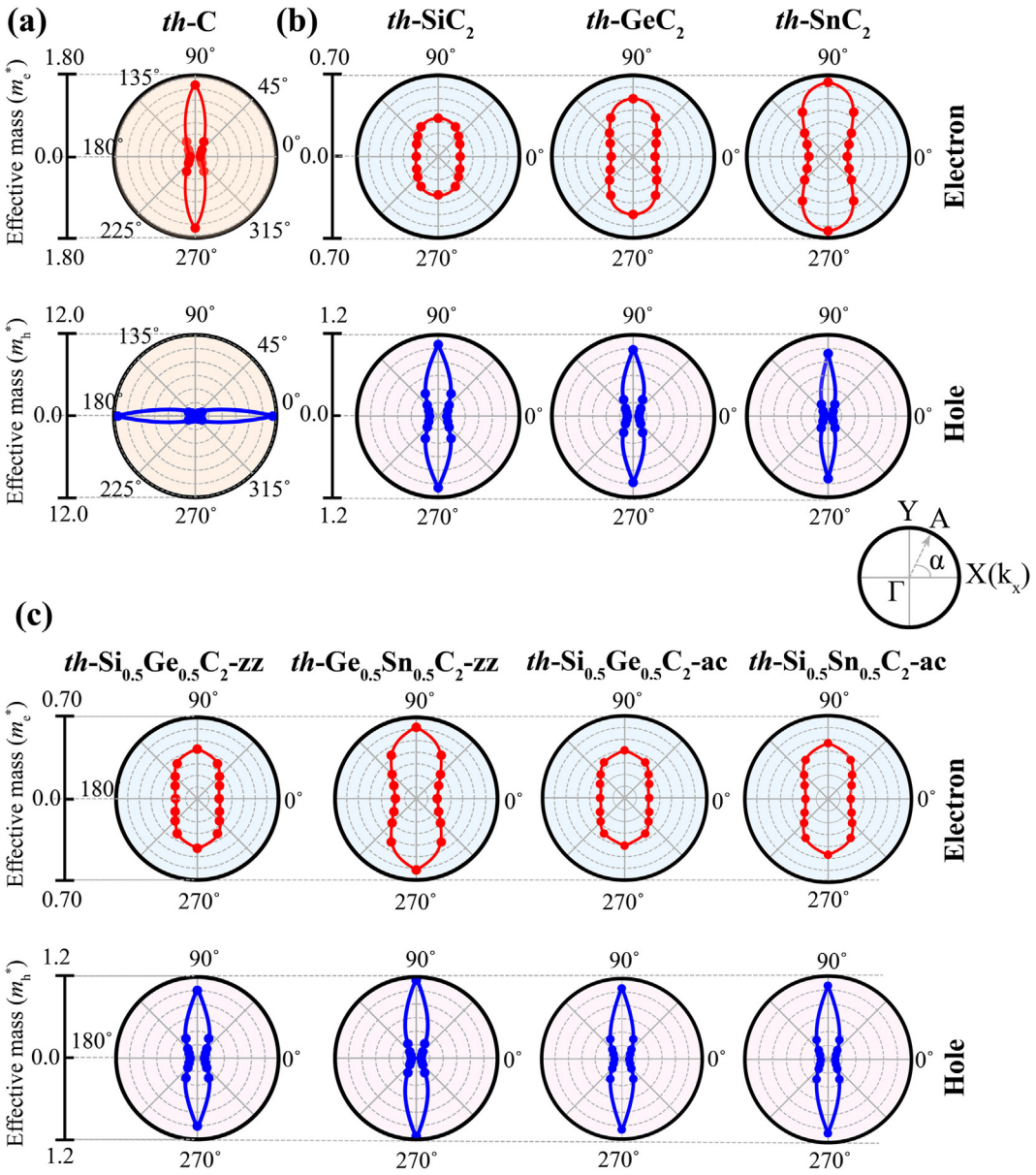

Fig. 7. Angular dependent effective mass of electrons and holes from the Γ-X direction to an arbitrary Γ-A direction for (a) *th*-C, (b) *th*-XC_2, and (c) ternary alloys. Unit of effective mass is in mass of a free electron (m_0). (A colour version of this figure can be viewed online.)

electron mass) are much lower than that along the Γ-Y (ranging from 0.92 m_0 to 1.15 m_0), indicating remarkable anisotropic feature in the carrier effective mass. Likewise, the electron effective mass along the Γ-X (ranging from 0.16 m_0 to 0.20 m_0) are relatively lower than that along the Γ-Y (ranging from 0.33 m_0 to 0.64 m_0). Importantly, the hole effective mass of *th*-XC_2 carbides along the transport direction (Γ-X) is considerably lower than that of *th*-C about 0.31 m_0 along the transport direction (Γ-Y). Moreover, the electron effective mass of *th*-XC_2 carbides along the transport direction (Γ-X) is almost same as that of *th*-*C* about 0.11 m_0 along the transport direction (Γ-X).

We further calculated the carrier mobility (μ) of the 2D carbides along the zigzag and armchair directions at $T = 300$ K. The carrier mobility of the 2D materials usually estimated according to the formula as $\mu_i = \frac{eh^3 C_i}{(2\pi)^3 k_B T m_i^* m_d E_{1i}^2}$ where i is the transport direction, m_i^* is the effective mass along the transport direction i, m_d is the average effective mass, defined as $m_d = \sqrt{m_x^* m_y^*}$, E_{1i} is the deformation potential, defines as $E_{1i} = \Delta E/(\Delta l/l_0)$ where ΔE is the energy change of the VBM and CBM bands under small lattice strain. We computed the deformation potentials by fitting the variation of band edge energies with respect to vacuum level as a function of the small lattice strain ($\Delta l/l_0 \sim \pm 0.5\%$), l_0 is the unstrained lattice constant along the transport direction i), and presented in Fig. S9 and Fig. S10 of Supporting Information, and listed in Table 3. We note that the electron mobility of *th*-XC_2 carbides, especially Ge- and Sn-based 2D carbides, is extraordinarily high (0.43×10^5 $cm^2V^{-1}s^{-1}$ for *th*-GeC_2, 0.40×10^5 $cm^2V^{-1}s^{-1}$ for *th*-SnC_2, 0.11×10^5 $cm^2V^{-1}s^{-1}$ for *th*-$Si_{0.5}Ge_{0.5}C_2$-zz, 7.1×10^5 $cm^2V^{-1}s^{-1}$ for *th*-$Ge_{0.5}Sn_{0.5}C_2$-zz, and $0.1 \times 10^5 cm^2V^{-1}s^{-1}$ for *th*-$Si_{0.5}Ge_{0.5}C_2$-ac) because of the small effective mass and deformation constants (weak electron-phonon scattering). The electron mobility of *th*-GeC_2, *th*-SnC_2, and *th*-$Ge_{0.5}Sn_{0.5}C_2Ge_{0.5}Sn_{0.5}C_2$ is more than 39, 37,

Table 3
Carrier effective mass m^* (m_0 is the mass of free electron) along from Γ – X to Γ – A an arbitrary directions, deformation potential E_1, and carrier mobility μ^{2D} of *th*-C, *th*-XC_2, and ternary alloys along the zigzag (x) and armchair (y) directions at room temperature.

		Γ – X	Γ – A	Γ – A	Γ – A	Γ – Y				
		($\alpha = 0^\circ$)	($\alpha = 30^\circ$)	($\alpha = 45^\circ$)	($\alpha = 60^\circ$)	($\alpha = 90^\circ$)	E_1^x	E_1^y	μ_x^{2D}	μ_y^{2D}
		m_x^*/m_0	m^*/m_0	m^*/m_0	m^*/m_0	m_y^*/m_0	(eV)	(eV)	($cm^2V^{-1}s^{-1}\times10^3$)	
th-C	hole	11.44	1.15	0.61	0.42	0.31	4.60	4.81	0.01	0.44
	electron	0.11	0.15	0.21	0.38	1.58	5.08	2.23	5.16	1.83
th-SiC_2	hole	0.13	0.16	0.23	0.38	1.06	14.05	8.41	0.22	0.08
	electron	0.19	0.21	0.25	0.30	0.33	6.85	16.81	0.95	0.10
th-GeC_2	hole	0.09	0.11	0.16	0.28	0.98	11.95	4.63	0.70	0.38
	electron	0.19	0.23	0.29	0.39	0.50	1.03	14.91	42.96	0.07
th-SnC_2	hole	0.06	0.07	0.11	0.20	0.92	9.62	4.86	1.45	0.29
	electron	0.16	0.21	0.28	0.44	0.64	0.95	13.17	40.91	0.04
th-$Si_{0.5}Ge_{0.5}C_2$-zz	hole	0.11	0.14	0.20	0.34	1.00	13.14	5.94	0.38	0.19
	electron	0.19	0.22	0.27	0.35	0.43	1.98	15.37	11.28	0.07
th-$Ge_{0.5}Sn_{0.5}C_2$-zz	hole	0.07	0.09	0.13	0.25	1.15	10.40	4.97	0.95	0.21
	electron	0.18	0.22	0.29	0.43	0.61	0.22	13.92	705.63	0.04
th-$Si_{0.5}Ge_{0.5}C_2$-ac	hole	0.11	0.14	0.20	0.34	1.05	12.40	6.30	0.41	0.15
	electron	0.20	0.24	0.28	0.35	0.41	2.12	15.12	9.17	0.08
th-$Si_{0.5}Sn_{0.5}C_2$-ac	hole	0.10	0.13	0.19	0.32	1.06	10.45	5.77	0.60	0.16
	electron	0.19	0.23	0.28	0.38	0.47	2.49	14.16	6.05	0.06

and 640 times that of black phosphorus (1100–1140 $cm^2V^{-1}s^{-1}$) [60] while their hole mobility is more than 3.5, 7.2, and 4.8 times that of monolayer MoS_2 (200–270 $cm^2V^{-1}s^{-1}$) [61], respectively. Thus, the sizable direct band gaps, ultrahigh high carrier mobilities with low effective mass, and strong anisotropic mechanical and electronic properties make *th*-XC_2 carbides so attractive for nanoelectronics and optoelectronics.

4. Conclusions

We have explored a new type of 2D group-IV carbides composed of X (Si, Ge, Sn) atoms and C=C dimers. Using the state-of-the-art *ab-initio* calculations, we have ensured that the predicted 2D carbides are energetically favorable and exhibit the strong stabilities based on the dynamical, thermal, and mechanical stability analysis. Due to the unique atomic configuration with C_2 dimers, they have showed remarkable phononic gaps. The width and position of the phonon gap can be modulated by hybridization and alloying. The feature of tunable phononic band gap can be potentially useful for thermoelectric applications. The alloying of the 2D carbides offers the ability to tailor the structural, mechanical, and electronic properties. They exhibit remarkable mechanical properties, including, the anisotropic mechanical response, flexibility, and ideal strength. They are semiconductors with a narrow direct band gaps which can be continuously tuned by strain and alloy engineering. They have showed excellent transport properties including strong anisotropic effective mass and ultrahigh (up to $\sim 10^5$ $cm^2V^{-1}s^{-1}$) carrier mobility. More interestingly, the anisotropy of the hole effective mass can be rotated by 90° simply by alloying X element in *th*-C. Thus, the intrinsic carrier mobility in *th*-C is significantly enhanced by not only strain but also alloy engineering. The sizable direct band gaps, high carrier mobilities, and anisotropic properties make the 2D carbides extremely attractive nanomaterials for nanoelectronics.

CRediT authorship contribution statement

Mehmet Emin Kilic: Conceptualization, Investigation, Writing – original draft, Writing – review & editing, Visualization. **Kwang-Ryeol Lee:** Supervision, Writing – review & editing.

Declaration of competing interest

The authors declare that they have no known competing financial interests or personal relationships that could have appeared to influence the work reported in this paper.

Acknowledgment

This work was supported by Brain Pool Program through the National Research Foundation of Korea (NRF) funded by the Ministry of Science and ICT (2020H1D3A1A02081517) and the Nano Materials Research Program through the Ministry of Science and IT Technology under project No. NRF-2016M3A7B4025402.

Appendix A. Supplementary data

Supplementary data to this article can be found online at https://doi.org/10.1016/j.carbon.2021.04.092.

Supporting Information

Optimized atomic structure, dynamics stability, electronic band structure, and Stone-Wales transformation of *penta*-SiC_2; atomic structure of silagraphene; AIMD results; Strain energy with respect to strain; Strain-stress curves; Projected density-of-states (pDOS); Charge density of the VBM and CBM; ELF plot; Deformation potential energy with respect to strain.

References

[1] K.S. Novoselov, A.K. Geim, S.V. Morozov, D. Jiang, Y. Zhang, S.V. Dubonos, I.V. Grigorieva, A.A. Firsov, Electric field effect in atomically thin carbon films, Science 306 (5696) (2004) 666–669.
[2] X. Zhang, Z. Lai, Q. Ma, H. Zhang, Novel structured transition metal dichalcogenide nanosheets, Chem. Soc. Rev. 47 (9) (2018) 3301–3338.
[3] S. Ipek, M. Kilic, A. Mogulkoc, S. Cahangirov, E. Durgun, Semiconducting defect-free polymorph of borophene: peierls distortion in two dimensions, Phys. Rev. B 98 (24) (2018) 241408.
[4] L.H. Li, Y. Chen, Atomically thin boron nitride: unique properties and applications, Adv. Funct. Mater. 26 (16) (2016) 2594–2608.
[5] P. Vogt, P. De Padova, C. Quaresima, J. Avila, E. Frantzeskakis, M.C. Asensio, A. Resta, B. Ealet, G. Le Lay, Silicene: compelling experimental evidence for graphenelike two-dimensional silicon, Phys. Rev. Lett. 108 (15) (2012) 155501.
[6] L. Li, Y. Yu, G.J. Ye, Q. Ge, X. Ou, H. Wu, D. Feng, X.H. Chen, Y. Zhang, Black phosphorus field-effect transistors, Nat. Nanotechnol. 9 (5) (2014) 372.
[7] H. Şahin, S. Cahangirov, M. Topsakal, E. Bekaroglu, E. Akturk, R.T. Senger,

S. Ciraci, Monolayer honeycomb structures of group-IV elements and III-V binary compounds: first-principles calculations, Phys. Rev. B 80 (15) (2009) 155453.
[8] F. Ersan, A.G. Gökçe, E. Aktürk, Point defects in hexagonal germanium carbide monolayer: a first-principles calculation, Appl. Surf. Sci. 389 (2016) 1–6.
[9] A.G. Gökçe, F. Ersan, Adsorption of alkali and alkaline earth metal atoms and dimers on monolayer germanium carbide, Philos. Mag. 97 (3) (2017) 155–167.
[10] Y. Mogulkoc, M. Modarresi, A. Mogulkoc, Y. Ciftci, B. Alkan, First principle and tight-binding study of strained SnC, J. Phys. Chem. Solid. 111 (2017) 458–463.
[11] L.-J. Zhou, Y.-F. Zhang, L.-M. Wu, SiC2 siligraphene and nanotubes: novel donor materials in excitonic solar cells, Nano Lett. 13 (11) (2013) 5431–5436.
[12] Z. Shi, Z. Zhang, A. Kutana, B.I. Yakobson, Predicting two-dimensional silicon carbide monolayers, ACS Nano 9 (10) (2015) 9802–9809.
[13] S. Lin, Light-emitting two-dimensional ultrathin silicon carbide, J. Phys. Chem. C 116 (6) (2012) 3951–3955.
[14] J. Liu, C. He, N. Jiao, H. Xiao, K. Zhang, R. Wang, L. Sun, Novel Two-Dimensional SiC2 Sheet with Full Pentagon Network, arXiv preprint arXiv:1307.6324.
[15] Y. Li, F. Li, Z. Zhou, Z. Chen, SiC2 silagraphene and its one-dimensional derivatives: where planar tetracoordinate silicon happens, J. Am. Chem. Soc. 133 (4) (2011) 900–908.
[16] H. Dong, L. Zhou, T. Frauenheim, T. Hou, S.-T. Lee, Y. Li, SiC7 siligraphene: a novel donor material with extraordinary sunlight absorption, Nanoscale 8 (13) (2016) 6994–6999.
[17] F. Calvo, S. Diaz-Tendero, M.-A. Lebeault, Translational, rotational and vibrational energy partitioning in the sequential loss of carbon dimers from fullerenes, Phys. Chem. Chem. Phys. 11 (30) (2009) 6345–6352.
[18] Q. Wang, M.-F. Ng, S.-W. Yang, Y. Yang, Y. Chen, The mechanism of single-walled carbon nanotube growth and chirality selection induced by carbon atom and dimer addition, ACS Nano 4 (2) (2010) 939–946.
[19] M. Sternberg, P. Zapol, L.A. Curtiss, Carbon dimers on the diamond (100) surface: growth and nucleation, Phys. Rev. B 68 (20) (2003) 205330.
[20] B. Guo, K. Kerns, A. Castleman, Ti8C12+-metallo-carbohedrenes: a new class of molecular clusters? Science 255 (5050) (1992) 1411–1413.
[21] M.-M. Rohmer, M. Bénard, J.-M. Poblet, Structure, reactivity, and growth pathways of metallocarbohedrenes M8C12 and transition metal/carbon clusters and nanocrystals: a challenge to computational chemistry, Chem. Rev. 100 (2) (2000) 495–542.
[22] T. Zhao, S. Zhang, Y. Guo, Q. Wang, TiC2: a new two-dimensional sheet beyond MXenes, Nanoscale 8 (1) (2016) 233–242.
[23] T. Zhao, J. Zhou, Q. Wang, Y. Kawazoe, P. Jena, Ferromagnetic and half-metallic FeC2 monolayer containing C2 dimers, ACS Appl. Mater. Interfaces 8 (39) (2016) 26207–26212.
[24] J.-O. Joswig, M. Springborg, The influence of C2 dimers on the stability of Ti(m)C(n) metcar clusters, J. Chem. Phys. 129 (13) (2008) 134311.
[25] B. Ram, H. Mizuseki, Tetrahexcarbon: a two-dimensional allotrope of carbon, Carbon 137 (2018) 266–273.
[26] F.M. de Vasconcelos, A.G. Souza Filho, V. Meunier, E.C. Girão, Electronic properties of tetragraphene nanoribbons, Phys. Rev. Mater. 3 (6) (2019), 066002.
[27] M.E. Kilic, K.-R. Lee, Tuning the electronic, mechanical, thermal, and optical properties of tetrahexcarbon via hydrogenation, Carbon 161 (2020) 71.
[28] M.E. Kilic, K.-R. Lee, Tetrahex carbides: two-dimensional group-IV materials for nanoelectronics and photocatalytic water splitting, Carbon 174 (2021) 368–381.
[29] J.P. Perdew, K. Burke, M. Ernzerhof, Generalized gradient approximation made simple, Phys. Rev. Lett. 77 (18) (1996) 3865.
[30] G. Kresse, J. Hafner, Norm-conserving and ultrasoft pseudopotentials for first-row and transition elements, J. Phys. Condens. Matter 6 (40) (1994) 8245.
[31] P.E. Blöchl, Projector augmented-wave method, Phys. Rev. B 50 (24) (1994) 17953.
[32] G. Kresse, D. Joubert, From ultrasoft pseudopotentials to the projector augmented-wave method, Phys. Rev. B 59 (3) (1999) 1758.
[33] H.J. Monkhorst, J.D. Pack, Special points for Brillouin-zone integrations, Phys. Rev. B 13 (12) (1976) 5188.
[34] J. Heyd, G.E. Scuseria, M. Ernzerhof, Hybrid functionals based on a screened coulomb potential, J. Chem. Phys. 118 (18) (2003) 8207–8215.
[35] J. Paier, M. Marsman, K. Hummer, G. Kresse, I.C. Gerber, J.G. Ángyán, Screened hybrid density functionals applied to solids, J. Chem. Phys. 124 (15) (2006) 154709.
[36] L. Chaput, A. Togo, I. Tanaka, G. Hug, Phonon-phonon interactions in transition metals, Phys. Rev. B 84 (9) (2011), 094302.
[37] S. Nosé, A unified formulation of the constant temperature molecular dynamics methods, J. Chem. Phys. 81 (1) (1984) 511–519.
[38] S. Nosé, A molecular dynamics method for simulations in the canonical ensemble, Mol. Phys. 52 (2) (1984) 255–268.
[39] W.G. Hoover, Canonical dynamics: equilibrium phase-space distributions, Phys. Rev. 31 (3) (1985) 1695.
[40] G. Henkelman, B.P. Uberuaga, H. Jónsson, A climbing image nudged elastic band method for finding saddle points and minimum energy paths, J. Chem. Phys. 113 (22) (2000) 9901–9904.
[41] D. Fan, S. Lu, Y. Guo, X. Hu, Novel bonding patterns and optoelectronic properties of the two-dimensional si_xc_ymonolayers, J. Mater. Chem. C 5 (14) (2017) 3561–3567.
[42] C. Zhang, S. Zhang, Q. Wang, Bonding-restricted structure search for novel 2D materials with dispersed $c_2$dimers, Sci. Rep. 6 (1) (2016) 1–11.
[43] J. Escudié, C. Couret, H. Ranaivonjatovo, Silenes SiC, germenes GeC and stannenes SnC : the French contribution, Coord. Chem. Rev. 178 (1998) 565–592.
[44] H.F. Bettinger, B.I. Yakobson, G.E. Scuseria, Scratching the surface of buckminsterfullerene: the barriers for Stone–Wales transformation through symmetric and asymmetric transition states, J. Am. Chem. Soc. 125 (18) (2003) 5572–5580.
[45] L. Li, S. Reich, J. Robertson, Defect energies of graphite: density-functional calculations, Phys. Rev. B 72 (18) (2005) 184109.
[46] Z. Slanina, X. Zhao, F. Uhlık, M. Ozawa, E. Osawa, Computational modeling of the elemental catalysis in the Stone–Wales fullerene rearrangements, J. Organomet. Chem. 599 (1) (2000) 57–61.
[47] B. Eggen, M. Heggie, G. Jungnickel, C. Latham, R. Jones, P. Briddon, Autocatalysis during fullerene growth, Science 272 (5258) (1996) 87–90.
[48] W.I. Choi, G. Kim, S. Han, J. Ihm, Reduction of activation energy barrier of Stone–Wales transformation in endohedral metallofullerenes, Phys. Rev. B 73 (11) (2006) 113406.
[49] G. Li, Y. Li, H. Liu, Y. Guo, Y. Li, D. Zhu, Architecture of graphdiyne nanoscale films, ChemComm 46 (19) (2010) 3256–3258.
[50] S. Zhang, J. Zhou, Q. Wang, X. Chen, Y. Kawazoe, P. Jena, Penta-graphene: a new carbon allotrope, Proc. Natl. Acad. Sci. U.S.A. 112 (8) (2015) 2372–2377.
[51] M.E. Kilic, K.-R. Lee, Novel two-dimensional tetrahexagonal boron nitride with sizable bandgap and sign-tunable Poisson's ratio, Nanoscale (2021), https://doi.org/10.1039/D1NR00734C.
[52] M.E. Kilic, K.-R. Lee, First-principles study of fluorinated tetrahexcarbon: stable configurations, thermal, mechanical, and electronic properties, J. Phys. Chem. C 124 (2020) 8225.
[53] A. Sgouros, M. Sigalas, G. Kalosakas, K. Papagelis, N. Papanicolaou, Phononic band gap engineering in graphene, J. Appl. Phys. 112 (9) (2012), 094307.
[54] M. Born, K. Huang, Dynamical Theory of Crystal Lattices, 1954. Oxford.
[55] M.E. Kilic, K.-R. Lee, Auxetic, flexible, and strain-tunable two-dimensional th-AlN for photocatalytic visible light water splitting with anisotropic high carrier mobility, J. Mater. Chem. C 9 (2021) 4971–4977.
[56] M.E. Kilic, S. Erkoc, Molecular dynamics simulations of zinc oxide nanostructures under strain: I-nanoribbons, J. Comput. Theor. Nanosci. 10 (1) (2013) 104–111.
[57] M.E. Kilic, S. Erkoc, Molecular dynamics simulations of ZnO nanostructures under strain: II-nanorods, J. Comput. Theor. Nanosci. 10 (1) (2013) 112–118.
[58] Z. Zhu, Y. Cheng, U. Schwingenschlögl, Band inversion mechanism in topological insulators: a guideline for materials design, Phys. Rev. B 85 (23) (2012) 235401.
[59] X. Peng, Q. Wei, G. Yang, Enhanced carrier mobility in anisotropic two-dimensional tetrahex-carbon through strain engineering, Carbon 165 (2020) 37–44.
[60] J. Qiao, X. Kong, Z.-X. Hu, F. Yang, W. Ji, High-mobility transport anisotropy and linear dichroism in few-layer black phosphorus, Nat. Commun. 5 (1) (2014) 1–7.
[61] Z. Jin, X. Li, J.T. Mullen, K.W. Kim, Intrinsic transport properties of electrons and holes in monolayer transition-metal dichalcogenides, Phys. Rev. B 90 (4) (2014), 045422.